Acoustic pressure field estimation methods for synthetic schlieren tomography

Eero Koponen,[a)] Jarkko Leskinen, Tanja Tarvainen,[b] and Aki Pulkkinen

Department of Applied Physics, University of Eastern Finland, P.O. Box 1627, 70211 Kuopio, Finland

(Dated: 18 March 2019)

Synthetic schlieren tomography is a recently proposed three-dimensional optical imaging technique for studying ultrasound fields. The imaging setup is composed of an imaged target, a water tank, a camera, and a pulsed light source that is stroboscopically synchronized with an ultrasound transducer to achieve tomographically stationary imaging of an ultrasound field. In this technique, ultrasound waves change the propagation of light rays by inducing a change in refractive index via acousto-optic effect. The change manifests as optical flow in the imaged target. By performing the imaging in a tomographic fashion, the two-dimensional tomographic dataset of the optical flow can be transformed into a three-dimensional ultrasound field. In this work, two approaches for acoustic pressure field estimation are introduced. The approaches are based on optical and potential flow regularized least square optimizations where regularization based on the Helmholtz equation is introduced. The methods are validated via simulations in a telecentric setup and are compared quantitatively and qualitatively to a previously introduced method. Cases of a focused, an obliquely propagating, and a standing wave ultrasound fields are considered. The simulations demonstrate efficiency of the introduced methods also in situations in which the previously applied method has weaknesses.

[a)] eero.koponen@uef.fi

[b] Also at: Department of Computer Science, University College London, Gower Street, London WCIE 6BT, United Kingdom.

I. INTRODUCTION

Ultrasound imaging is a fundamental part of medical diagnostics.[1] In addition to diagnostics, ultrasound has therapy applications, such as, treatment of cancer[2] and essential tremor[3] and targeted drug delivery.[4] To guarantee patient safety and quality of diagnostics or therapy, ultrasound devices need to be calibrated. This requires measurement of the ultrasound field, commonly accomplished using cumbersome and time-consuming hydrophone measurements.[5,6] Thus, calibration and quality assurance of ultrasound devices could benefit from new ultrasound measurement and characterization techniques.

Various optical imaging methods, namely schlieren imaging[7–9] and its variations, such as shadowgraphy,[10–12] background oriented schlieren (BOS) imaging,[13–15] and synthetic schlieren,[16–18] have been applied in imaging of pressure fields. Thus, they can potentially serve as alternatives for traditional measurement methods to characterize ultrasound fields. These methods rely on observing deflection of light passing through a heterogeneous refractive index field that carries information of a density or a pressure field.[19,20] In schlieren imaging, deflection of light is observed accurately using an expensive lens setup and an optical stop blocking non-deflected light arriving to a camera.[19,21] In the simplest variation, shadowgraphy, no optical setup is needed and the light is simply projected to a screen.[20] The deflected light is then observed as intensity variations. Shadowgraphy is mainly used for qualitative inspection of an ultrasound field due to its lack of sensitivity[19] and challenges in obtaining absolute pressure values.[10,11] The more recent schlieren variations are BOS[22] and synthetic schlieren[23] that use inexpensive and easy-to-use setups. In these methods, deflection of light is observed as optical distortions in an imaged target and thus, they can produce quantitative measurements after post-processing of the images. In ultrasound community, both BOS and synthetic schlieren methodologies have been used in imaging of ultrasound fields.[14,17,18]

In synthetic schlieren tomography (SST) for imaging of ultrasound fields, refractive index field distribution is induced via acousto-optic effect.[18] This results in light rays travelling curved paths through the heterogeneous refractive index field, causing optical distortions in an imaged target. Various optical flow methods exist to determine optical displacements (gradient projections) from the captured images, such as Lucas-Kanade,[24] Horn-Schunck (HS),[25] and cross correlation-methods.[15,26] Of these methods, HS has good quality and accuracy.[27] In addition, potential flow[28] can be used to determine potential functions (projections) of a pressure field. Since the determined optical distortions are two-dimensional (2D), a tomographic dataset is required for reconstructing a three-dimensional (3D) ultrasound field. In SST, an ultrasound field is imaged stationarily using a stroboscopic setup based on synchronizing a pulsed light source with the refractive index perturbations. Tomographic imaging is achieved by rotating the refractive index field or the camera, the light source, and the imaged target.

In this work, two new approaches for estimating acoustic pressure fields in SST are introduced. The approaches are based on the optical and potential flow problems, which are solved using a regularized least squares in a form similar to HS. For the regularizations, Laplace and Helmholtz equations are applied. The estimated flow solutions are then used with an inverse Radon transform to obtain estimates of the pressure field. The approaches

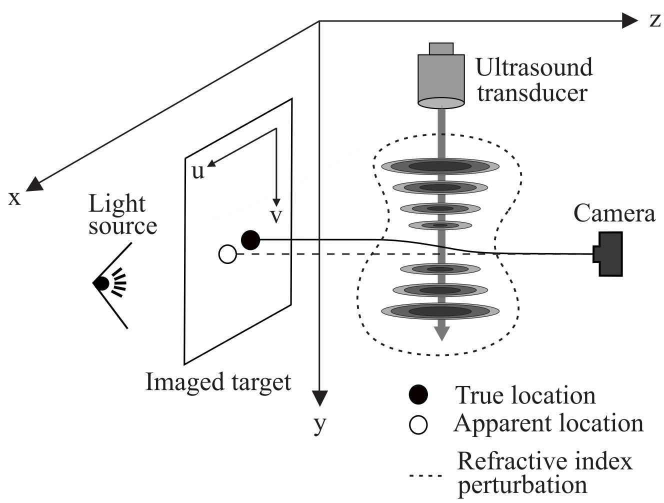

FIG. 1. Schematic image of a synthetic schlieren setup.

are compared to the previously introduced method using numerical simulations in qualitative and quantitative fashion. Comparison is conducted using three ultrasound fields that represent real measurement scenarios: a focused, an obliquely propagating focused, and a standing wave ultrasound fields.

II. MATERIALS AND METHODS

In this work, a SST setup consisting of a stationary ultrasound transducer and a rotating camera, a light source, and an imaged target all immersed in the imaging medium is considered. A schematic image of such a setup is shown in Fig. 1. The camera is modelled as telecentric, meaning it performs imaging using orthographic view with respect to the captured light rays that all propagate in parallel. The coordinate system described in the Fig. 1 is adapted throughout this work.

A. Theory of SST

In a simple medium, such as water, refractive index of light behaves linearly as a function of adiabatic pressure due to the acousto-optic effect[29,30]

$$n(x, y, z) = n_0 + \left(\frac{\partial n}{\partial p}\right) p(x, y, z), \tag{1}$$

where n_0 is the refractive index of the ambient medium, $(\partial n/\partial p)$ is the adiabatic piezo-optic coefficient,[29] and $p(x, y, z)$ is the acoustic pressure as a function of spatial coordinates (x, y, z).

Heterogeneous refractive index field results in curving of light rays passing through it. The path of a light ray, according to a ray equation[31] is

$$\frac{\mathrm{d}}{\mathrm{d}s}\left(n(\boldsymbol{\gamma}(s))\frac{\mathrm{d}\boldsymbol{\gamma}}{\mathrm{d}s}(s)\right) = \nabla n(\boldsymbol{\gamma}(s)), \tag{2}$$

where $\boldsymbol{\gamma}$ is an optical path vector and s is the geometrical length of the optical path. In general, the optical path is a complex curve and the ray equation is non-linear. However, for small refractive index perturbations, Eq. (2) can be linearized.[15,26,32] It follows that the propagation can be modelled as light rays experiencing a deflection that is proportional to the projection of the refractive index field gradient along a straight path through the perturbation. The linearized deflection angles can be expressed as

$$\begin{cases} \phi_x(x, y) = \dfrac{1}{n_0}\displaystyle\int_Z \frac{\partial n}{\partial x}(x, y, z)\mathrm{d}z, \\ \phi_y(x, y) = \dfrac{1}{n_0}\displaystyle\int_Z \frac{\partial n}{\partial y}(x, y, z)\mathrm{d}z, \end{cases} \tag{3}$$

where $\phi_x(x, y)$ is the horizontal and $\phi_y(x, y)$ is the vertical deflection angle towards x and y axes, and Z is the integration path over the width of refractive index perturbation. Within paraxial approximation, the displacement of the light ray originating from $(x, y, z = 0)$ can be expressed as

$$\begin{cases} u(x, y) = D\phi_x(x, y), \\ v(x, y) = D\phi_y(x, y), \end{cases} \tag{4}$$

where $u(x, y)$ is the horizontal and $v(x, y)$ is the vertical displacement, and D is the distance between the thin schlieren object and the camera. The relations for displacements and pressure gradient are obtained by combining Eqs. (1)–(4)

$$\begin{cases} u(x, y) = \kappa \int_Z \frac{\partial p}{\partial x}(x, y, z)\mathrm{d}z, \\ v(x, y) = \kappa \int_Z \frac{\partial p}{\partial y}(x, y, z)\mathrm{d}z, \end{cases} \tag{5}$$

where $\kappa = (D/n_0)(\partial n/\partial p)$ is a factor relating the line integral of the pressure gradient projections to absolute displacements. In the above formulations (1)–(5), we have assumed that the light pulses are infinitely short and the light ray propagation through the perturbed water is instantaneous. These assumptions are reasonable since the speed of light in water is much faster than the speed of ultrasound, hence the change in the refractive index is negligible during the propagation of a light pulse.

The optical displacements can be determined from a non-perturbed image, $I(x, y)$, and the perturbed image, $I^\delta(x, y)$ assuming the same exposure and illumination conditions. The relation between these images holds that[33]

$$I^\delta(x, y) = I(x + u(x, y), y + v(x, y)), \tag{6}$$

where $(x + u(x, y), y + v(x, y))$ is an absolute position of a displaced light ray.

B. Estimating optical flow

In this work, HS method is used for determining the optical displacements from the image distortions due to its good performance for continuous and smooth displacements under noisy conditions. In addition to the traditional HS,[25] a potential flow approach is also used.[28]

1. *Optical flow*

The traditional HS method is an approach for estimating the perturbed image with a first order truncated Taylor series as

$$\begin{aligned} I^\delta(x,y) &= I(x+u(x,y), y+v(x,y)) \\ &\approx I(x,y) + u(x,y)\frac{\partial I}{\partial x}(x,y) + v(x,y)\frac{\partial I}{\partial y}(x,y). \end{aligned} \tag{7}$$

Estimating the displacements is an ill-posed problem and has a non-unique solution due to more unknowns than equations. Uniqueness of a solution is obtainable by alleviating the ill-posedness via regularization.[34] Horn and Schunck introduced the unknown displacements as the minimizers of a global smoothness constraint.[25] In addition to a unique solution, the regularization fills in information from the neighbourhood at locations where the image gradient vanishes ($\nabla I \approx 0$). The HS regularized linear least squares problem in a continuous form is expressed as

$$\begin{aligned} (\hat{u}, \hat{v}) = \underset{(u,v)}{\arg\min} &\int_A \left(I^\delta - I - u\frac{\partial I}{\partial x} - v\frac{\partial I}{\partial y}\right)^2 \mathrm{d}x\mathrm{d}y \\ &+ \alpha^2 \int_A (\mathcal{L}u)^2 + (\mathcal{L}v)^2 \mathrm{d}x\mathrm{d}y, \end{aligned} \tag{8}$$

where $(\hat{u}, \hat{v})$ is an estimate of the image displacements, α is a regularization parameter, $\mathcal{L}$ is a regularization operator, and A is the surface area over which the integration is carried over. The regularization operator $\mathcal{L}$ is used to impose soft constraints on the estimates, thus making the problem less ill-posed. For smooth fields, first or second order differential operators are often used to impose differentiability of orders one and two.[25,33]

In practice, numerical solving of this regularized least squares problem requires disretization of the problem by expressing the images and displacements as vectors that compose of pixel intensities. Images and displacements expressed as vectors are $\boldsymbol{I} = (I_1, ..., I_J)^\top$, $\boldsymbol{I^\delta} = (I_1^\delta, ...I_J^\delta)^\top$, $\boldsymbol{u} = (u_1, ..., u_J)^\top$, and $\boldsymbol{v} = (v_1, ..., v_J)^\top$, where I_j and I_j^δ are the pixel intensities of unperturbed and perturbed images, and u_j and v_j are the horizontal and vertical displacements, for pixels $j = 1, ..., J$. The discrete regularized least squares can then be expressed as

$$\begin{aligned}(\hat{\boldsymbol{u}}, \hat{\boldsymbol{v}}) = \underset{(\boldsymbol{u},\boldsymbol{v})}{\arg\min} \big|\big|\boldsymbol{I}^\delta - \boldsymbol{I} - \mathbf{D}_x\boldsymbol{u} - \mathbf{D}_y\boldsymbol{v}\big|\big|^2 \\ + \alpha^2\big(\big|\big|\mathbf{L}\boldsymbol{u}\big|\big|^2 + \big|\big|\mathbf{L}\boldsymbol{v}\big|\big|^2\big),\end{aligned} \tag{9}$$

where $||\cdot||$ is the Euclidean 2-norm, $\mathbf{D}_x = \mathrm{diag}\{I_{1,x}, ..., I_{J,x}\}$ and $\mathbf{D}_y = \mathrm{diag}\{I_{1,y}, ..., I_{J,y}\}$ are diagonal matrices of first order centered finite difference approximations[35] of the x and y derivatives of $\boldsymbol{I}$ for pixels j, and $\mathbf{L}$ is a regularization matrix (see Sec. II B 3). For details on solving least squares optimization problems of form Eq. (9), see e.g. Ref.[34,36]

2. *Potential flow*

In potential flow method, the optical flow fields in Eq. (5) are described as a gradient of a potential function

$$P = \kappa \int_Z p(x, y, z)\mathrm{d}z, \tag{10}$$

such that $(u, v) = \nabla P$ and the regularized least squares problem (8) then becomes

$$\begin{aligned}\hat{P} = \arg\min_P \int_A \Big(I^\delta - I - \Big(\frac{\partial I}{\partial x}\frac{\partial}{\partial x} \\ + \frac{\partial I}{\partial y}\frac{\partial}{\partial y}\Big)P\Big)^2 \mathrm{d}x\mathrm{d}y + \alpha^2 \int_A (\mathcal{L}P)^2 \mathrm{d}x\mathrm{d}y.\end{aligned} \tag{11}$$

The problem in a discrete form is

$$\begin{aligned}\hat{\boldsymbol{P}} = \arg\min_{\boldsymbol{P}} \big|\big|\boldsymbol{I}^\delta - \boldsymbol{I} - \big(\mathbf{D}_x\mathbf{G}_x + \mathbf{D}_y\mathbf{G}_y\big)\boldsymbol{P}\big|\big|^2 \\ + \alpha^2\big|\big|\mathbf{L}\boldsymbol{P}\big|\big|^2,\end{aligned} \tag{12}$$

where $\boldsymbol{P} = (P_1, ..., P_J)^\top$ is the potential function in vector form, and $\mathbf{G}_x$ and $\mathbf{G}_y$ are the first order centered finite difference approximation operator matrices for the x and y derivatives. For details on solving least squares optimization problems of form Eq. (12), see e.g. Ref.[34,36] Because potential flow method estimates the potential function $\boldsymbol{P}$, the problem has equal number of unknowns and equations. However, regularization is still needed due to noise and zero image gradient locations ($\nabla \boldsymbol{I} \approx 0$).

3. *Regularization operator*

In this work, we use two different regularization operators. The first is a Laplace operator $\nabla^2 = \big(\frac{\partial^2}{\partial x^2} + \frac{\partial^2}{\partial y^2}\big)$ that promotes smooth solutions[25,33] of optimization problems (9) and (12). The second regularization operator $\nabla^2 + k^2$ is based on the Helmholtz equation for acoustic fields, where $k = 2\pi/\lambda = \omega/\text{c}$ is the wavenumber, λ is the wavelength, ω is the angular frequency, and c is the speed of sound of the acoustic field.[37] The operator promotes solutions with acoustic wave-like features. In discrete forms, Laplace and Helmholtz operators are expressed as

$$\nabla^2 \approx \quad \mathbf{G}_{xx} + \mathbf{G}_{yy} = \mathbf{L}, \tag{13}$$

$$\nabla^2 + k^2 \approx \mathbf{G}_{xx} + \mathbf{G}_{yy} + k^2\mathbf{I} = \mathbf{L}, \tag{14}$$

where $\mathbf{G}_{xx}$ and $\mathbf{G}_{yy}$ are matrix operators corresponding to second order centered finite difference approximations[38] of second partial derivatives along x- and y-axes, and $\mathbf{I}$ is an identity matrix, and $\mathbf{L}$ is a discrete regularization matrix. Since the optical flow fields in Eq. (5) can be expressed as the gradient of potential flow (10), imposing a second order differentiability with the regularization operators (13) and (14) causes a higher level differentiability assumption on the solution of optical flow (9) than potential flow (12).

C. Tomographic imaging

The principle of tomographic imaging in SST with a stationary ultrasound field and a rotating camera, a light source, and an imaged target is visualized in Fig. 2. Each of the captured images at different angles are 2D projections and carry information of the pressure field.

In order to describe the projections in tomographic coordinates, a mapping from the pressure fields' laboratory coordinates (x, y, z) to the local coordinates (x', y', z') of the rotating camera is needed. The angle of rotation θ around the y-axis connects the two

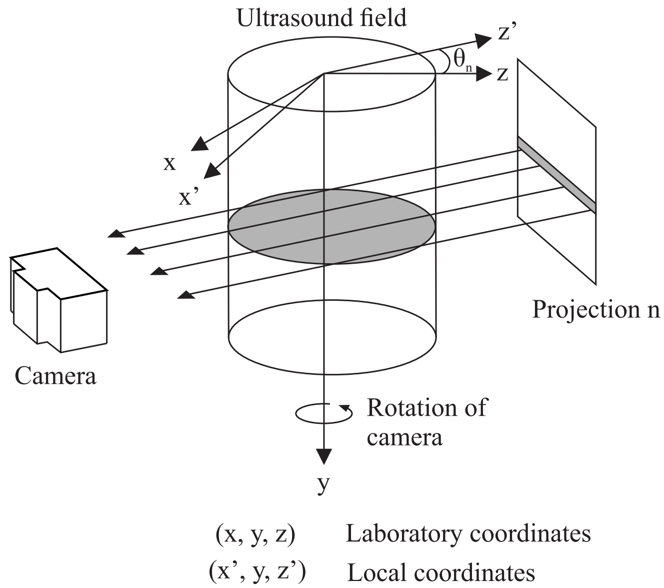

FIG. 2. Schematic image of measurement setup of SST. Laboratory coordinates (x, y, z) of the pressure field, local coordinates (x', y, z') of the rotating camera, and the imaged target at a projection angle θ_n.

coordinate systems

$$\begin{cases} x = x' \cos(\theta) - z' \sin(\theta), \\ y = y', \\ z = x' \sin(\theta) + z' \cos(\theta). \end{cases} \tag{15}$$

Expressing the line integral along the optical path over the pressure field in rotated coordinates is equivalent to a Radon transform[39,40] $\mathcal{R}\{\cdot\}(x', \theta)$ as

$$\mathcal{R}\{p(x, y, z)\}(x', \theta) = \int_{-\infty}^{\infty} p(x' \cos(\theta) - z' \sin(\theta), \\ y, x' \sin(\theta) + z' \cos(\theta)) \mathrm{d}z'. \tag{16}$$

Expressing the optical displacements of Eq. (5) and the potential function (10) similarly as the Radon transform (16) results in

$$u(x', y, \theta) = \kappa \frac{\partial}{\partial x'} \mathcal{R}\{p(x, y, z)\}(x', \theta), \tag{17}$$

$$v(x', y, \theta) = \kappa \frac{\partial}{\partial y'} \mathcal{R}\{p(x, y, z)\}(x', \theta), \tag{18}$$

$$P(x', y, \theta) = \kappa \mathcal{R}\{p(x, y, z)\}(x', \theta). \tag{19}$$

The above formulations (15)–(19) also apply to imaging with a rotating ultrasound field and a stationary camera, a light source, and an imaged target.

D. Tomographic pressure field estimations

The previous pressure field estimation method introduced in Ref.[18] uses the vertical displacement to form an estimate for the pressure. For completeness, the method is paraphrased here. According to Eq. (18), $v(x', y, \theta)$ is the Radon transform of the y-derivative of the pressure field. Hence, we can use an inverse Radon transform (filtered back-projection algorithm in practice[39,41]) to estimate the y-derivative of the pressure field. Furthermore, for strongly forward directed pressure fields, a plane-wave approximation can be made. In a lossless medium, the Helmholtz equation[37] is

$$\nabla^2 p + k^2 p = 0. \tag{20}$$

Assuming plane-wave propagation along the y-direction, the derivatives in x- and z-directions become negligible and an approximate wave-equation holds that

$$\frac{\partial^2 p}{\partial y^2} + k^2 p \approx 0, \tag{21}$$

from which a plane-wave approximation for the pressure can be obtained using

$$p = -\frac{c^2}{\omega^2}\frac{\partial}{\partial y}\Big(\frac{\partial p}{\partial y}\Big), \tag{22}$$

where $\partial p/\partial y$ can be obtained using the inverse Radon transform.[39,41] The pressure estimation can thus be expressed as

$$p(x, y, z) = -\frac{1}{\kappa}\frac{c^2}{\omega^2}\frac{\partial}{\partial y}\mathcal{R}^{-1}\{v(x', y, \theta)\}(x, z), \tag{23}$$

The approach (23) is referred to as pressure estimation based on the v-displacement (PE-v).

In this work, two new pressure field estimation methods are introduced. The first pressure estimation approach is based on the horizontal displacement $u(x', y, \theta)$. By integrating Eq. (17) along the x'-direction, we obtain

$$\begin{aligned} U(x'', y, \theta) &= \int_{-\infty}^{x''} u(x', y, \theta)\mathrm{d}x' \\ &= \kappa\mathcal{R}\{p(x, y, z)\}(x'', \theta), \end{aligned} \tag{24}$$

where $U(x'', y, \theta)$ is now a quantity related to the Radon transform of pressure field that can be readily obtained by applying the inverse Radon transform as

$$p(x, y, z) = \frac{1}{\kappa}\mathcal{R}^{-1}\{U(x'', y, \theta\}(x, z). \tag{25}$$

The approach (25) is referred to as pressure estimation based on the u-displacement (PE-u).

The second new approach uses the potential flow estimate (19) and the inverse Radon transform to obtain the pressure field as

$$p(x, y, z) = \frac{1}{\kappa}\mathcal{R}^{-1}\{P(x', y, \theta\}(x, z). \tag{26}$$

The approach (26) is referred to as pressure estimation based on the pressure potential function P (PE-P).

III. SIMULATION SETUP AND ANALYSIS

In this work, the simulation setup is telecentric, that is, the light rays travel along parallel lines from the light source to the camera. Tomographic imaging is achieved by rotating the camera, the light source and the imaged target over a span of 180° at 1° increments. All numerical computations were implemented in MATLAB R2017b (The MathWorks Inc., Natick, MA, USA).

A. Acoustic field simulations

Three acoustical simulation setups, shown in Fig. 3, were investigated: a focused ultrasound transducer sonicating along the rotation axis and obliquely at an angle of 45° with respect to the rotation axis, and a piston transducer sonicating along the rotation axis towards a reflecting target creating a standing wave. Both of the transducers were simulated at a medically relevant frequency of $f = 1.01$ MHz. The pressure fields were simulated in an isotropic medium using k-Wave[42] that is based on a k-space pseudospectral method for time domain acoustic simulations. The simulation parameters are shown in Table I.

In the focused acoustic field simulation, the geometrically focused transducer had an element diameter and a focal length of 45.2 mm similar to Ref.[18] The transducer operated in a burst mode of 50 cycles (49.5 μs burst duration, 73.6 mm propagation distance in water). A snapshot of the simulation was taken at a time point of 55.1 μs, corresponding to a sound burst being centered at the focus after a propagation distance of 82.0 mm. The size of the simulated acoustic field was 68.61 × 113.37 × 68.61 mm in (x, y, z) coordinates.

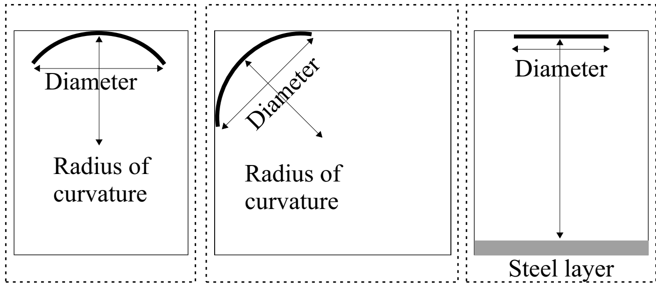

FIG. 3. Schematic image of simulation setups for a focused (left), an obliquely propagating focused (middle), and a standing wave (right) ultrasound fields. Borders of perfectly matched layers are shown by dashed lines.

The obliquely propagating focused ultrasound wave was obtained by rotating the focused ultrasound field by 45° with respect to the rotation axis.

In the standing wave-field simulation, the piston transducer had an element diameter of 12.5 mm and was driven with a continuous wave. A reflecting steel layer with thickness of 1.47 mm, corresponding to the wavelength of ultrasound, was simulated to be placed on the bottom of the domain, perpendicularly to the piston transducer. The distance between the steel layer and transducer was set to correspond a near-field length ($\frac{D^2}{4\lambda} \approx 26.6$ mm, where D is the diameter of the transducer). A snapshot of the standing wave was taken after the ultrasound's propagation distance of 2.5 times the near-field length, corresponding to 44.5 μs in time duration. The size of the simulated acoustic field was $28.12 \times 25.02 \times 25.02$ mm.

A perfectly matched layer of thickness $1.47 \times 2.94 \times 1.47$ mm was added outside the acoustic simulation domains to avoid unphysical reflections from the open simulation boundaries.

B. Optical simulations

The optical simulations were carried out in dense grids with $\Delta h = 24.54$ μm corresponding to 60 points per wavelength (PPW) similar in order of magnitude to Ref.[18] In order to perform the optical simulations, the simulated acoustic fields were interpolated to denser grids. Furthermore, to avoid unnecessarily large domains, they were cropped to smaller regions of interest. The acoustic field sizes were then $24.12 \times 38.84 \times 24.12$ mm, $24.42 \times 24.42 \times 24.12$ mm, and $25.00 \times 26.48 \times 25.00$ mm for the focused, the obliquely propagating, and the standing wave acoustic fields.

Furthermore, the linearized optical model assumes small optical displacements, and therefore the acoustic fields were normalized with the factor κ using Eqs. (23), (25), and (26) by limiting the maximum magnitude of the optical displacements to 4.4 μm (0.18 pixels).

Using the denser grid, an imaged target composed of individual Gaussian bumps was generated. The peak separation and cut-off width of the bumps were 368 μm (15 pixels) using a standard deviation of 147 μm (6 pixels). This corresponds to roughly four Gaussian bumps per wavelength of 1.47 mm (60 pixels) with intensity range from zero to one. The imaged targets were generated at sizes of 34.18×38.84 mm, 34.38×24.42 mm, and 35.41×26.48 mm for the focused, the obliquely propagating, and the standing wave acoustic fields. From these images, perturbed images were interpolated using a spline interpolation based on displacement fields computed using Eqs. (17)–(19).

In order to avoid performing an inverse crime,[43] the synthetic unperturbed and perturbed images were interpolated into new discretizations with a grid size of $\Delta h = 25.55$ μm. Additive and spatially uncorrelated normal distributed noise with a standard deviation of 0.01, corresponding to 1 % of the maximum intensity, was added to the intensity images.

The discretized regularization operators (13) and (14) explicitly include a homogeneous Dirichlet type boundary condition, causing the optical and potential flow estimates fall towards zero near the boundaries. To avoid this, the noisy unperturbed and perturbed images were zero padded in the y-direction. Following the optical and potential flow estimations, the estimated u, v, and P fields were cropped to regions of interest, which were used in analysis. For the focused, the obliquely propagating, and the standing wave fields, the sizes of the zero padded images were 34.18 × 44.95 mm, 34.38 × 30.52 mm, and 35.41 × 32.60 mm respectively. The corresponding sizes of regions of interest used in analysis were 28.05 × 38.83 mm, 28.25 × 24.4 mm, and 29.28 × 26.47 mm. The noisy unperturbed and perturbed images, and their difference image of the region of interest for the focused ultrasound field is shown in Fig. 4.

The pressure fields were estimated based on the optical and potential flow fields. The sizes of the estimated pressure fields were 24.1 × 44.95 × 24.1 mm, 24.40 × 30.52 × 24.12 mm, and 24.99 × 32.6 × 24.99 mm for the focused, the obliquely propagating, and the standing wave fields respectively. These estimates contained boundary artefacts arising from the optical and potential flow, and thus regions of interests of sizes 19.75 × 38.83 × 19.76 mm, 20.06 × 24.40 × 19.78 mm, and 20.65 × 26.47 × 20.65 mm for each of the fields was chosen for analysis.

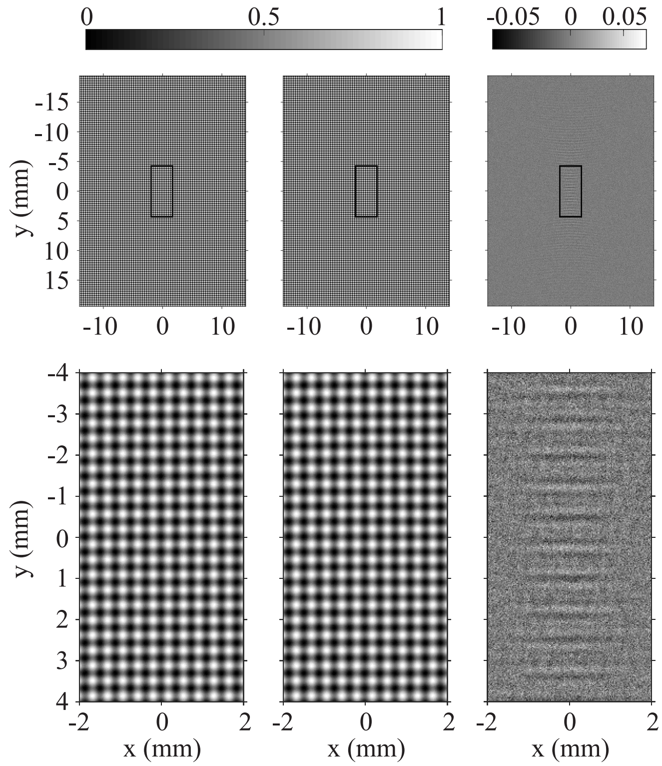

FIG. 4. From left to right: Noisy unperturbed, perturbed, and their difference image for the focused ultrasound field. Shown on the top row are the full-sized images and on the bottom row are the zoomed images.

C. Estimations and analysis

The optical flow displacements were estimated using the HS method (9) and the potential flow was estimated using Eq. (12) from the unperturbed and perturbed images. The regularization parameters for the optical and potential flow methods were chosen based on a qualitative inspection of the estimates at a range of different parameter values. The regularization parameter for the optical flow estimations was chosen separately for the pressure estimation approaches PE-v (23) and PE-u (25) in order to avoid favouring either of them. The optical flow estimates are referred to as vertical HS-v (18) and horizontal HS-u (17) displacements based on the separate HS estimations, and the potential function estimate is denoted as PF (19).

The optical and potential flow estimates were then used as an input in PE-v (23), PE-u (25), and PE-P (26) pressure estimation methods. The inverse Radon transform used in the estimation methods was performed using a Hamming-filtered back-projection algorithm that is suitable for noisy data. It was applied individually on the (x', θ)-planes for each y-slice and the reconstructed 2D pressure (x, z)-planes were then stacked in the y-direction to obtain the full 3D pressure field.

The optical and potential flow estimates, and the pressure estimates were analyzed using relative error (RE), expressed as

$$\mathrm{RE} = 100\% \cdot \frac{\|\hat{g} - g_{\mathrm{True}}\|}{\|g_{\mathrm{True}}\|}, \tag{27}$$

where $\hat{g}$ refers to either the estimated optical and potential flow components $\hat{u}$, $\hat{v}$, and $\hat{P}$, or to the estimated 3D pressure field $\hat{p}$, and g_{True} is the corresponding true field. Relative error was computed by interpolating the true displacement fields, pressure projection, and pressure fields into the discretization of the estimates. The boundary regions in the optical and potential flow estimates, and the corresponding boundary regions in the pressure estimates were excluded from the analyzes.

IV. RESULTS

A. Focused ultrasound field

Fig. 5 shows the true and the estimated optical flow fields HS-u, HS-v, and the potential flow estimate PF for the focused ultrasound field when using the Helmholtz regularization. The REs for the optical and potential flow estimates using the Laplace and the Helmholtz regularizations are shown in Table II. Based on the results, the optical and potential flow estimates are improved in comparison to the Laplace regularization, when the Helmholtz regularization is used. Of the Helmholtz regularization estimates, HS-v has the lowest RE followed by PF. They both have similar resemblance to their corresponding true fields. The high RE of HS-u is due to the acoustic field having smaller horizontal gradients than vertical, making it more ill-posed to estimate.

Fig. 6 shows the true pressure field, PE-u, PE-v, and PE-P estimates on the coronal planes yx ($z = 0$ mm) and the axial planes xz ($y = 0$ mm) when using the Helmholtz regularization. Table II shows REs of the estimates when using the Laplace and Helmholtz regularizations. Of the Helmholtz regularized pressure estimates, PE-u has the lowest RE, followed by PE-P. All the estimates seem similar and close to the true pressure values on the coronal plane. On the axial plane, pressure values of PE-P and PE-u are closer to the true values than PE-v that has smaller pressure values.

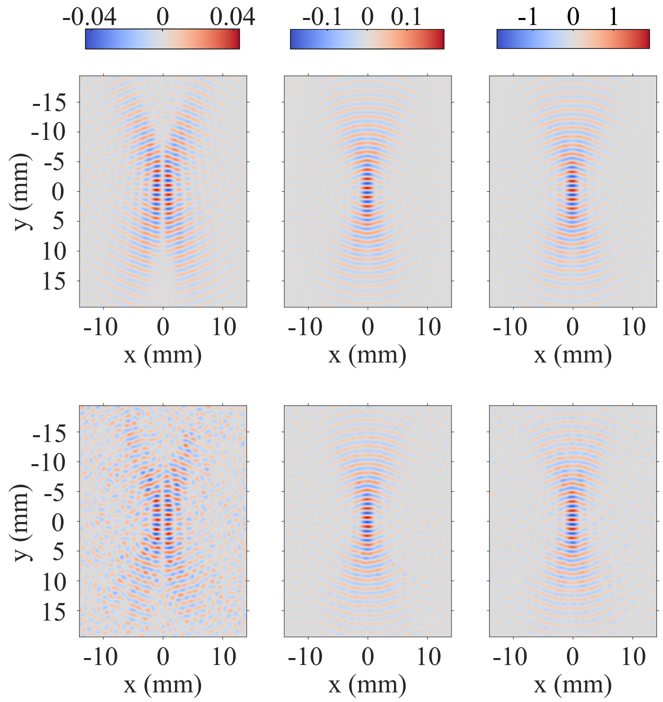

FIG. 5. (Color online) From left to right: the optical flow fields u and v, and the potential flow field P. Shown on the top are the true fields and on the bottom are the corresponding HS-u, HS-v, and PF estimates using the Helmholtz regularization. Fields are shown for the focused ultrasound field at a rotation angle of 45°. Colorbar units from left to right: m, m, and m^2.

B. Obliquely propagating focused ultrasound field

Fig. 7 shows the true and the estimated optical flow fields HS-u, HS-v, and the potential flow estimate PF for the obliquely propagating ultrasound field when using the Helmholtz regularization. The REs for the optical flow estimates using the Laplace and the Helmholtz regularizations are shown in Table II. Of the Helmholtz regularization estimates, HS-u and HS-v have similar REs and visual appearance due to the propagation angle of the ultrasound. The estimate PF has the lowest RE and the closest resemblance to its corresponding true field.

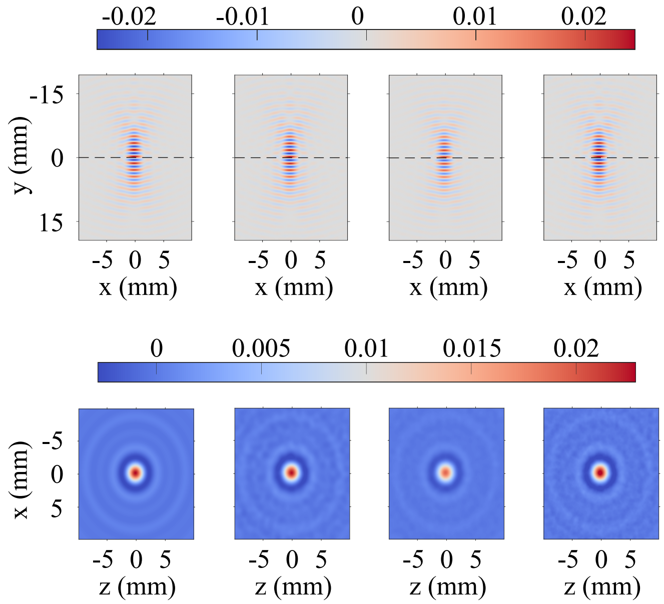

FIG. 6. (Color online) Coronal planes (top) and axial planes (bottom) of the focused ultrasound field. From left to right: true pressure field, PE-u, PE-v, and PE-P estimates when the Helmholtz regularization is used. Axial plane sections are shown by dashed lines on coronal planes. Colorbar units are in Pa.

Fig. 8 shows the true pressure field, PE-u, PE-v, and PE-P estimates on the coronal planes yx ($z = 0$ mm) and the axial planes xz ($y = 0$ mm) when using the Helmholtz regularization. Table II shows REs for the estimates when using the Laplace and Helmholtz regularizations. The Helmholtz regularized estimate PE-P has the lowest RE and resembles the true field the closest, followed by PE-u. In comparison to the results in Section IV A, the smaller focal pressure values of PE-v are more visible. These arise from the plane-wave approximation, that assumes propagation of sound principally along the y-axis.

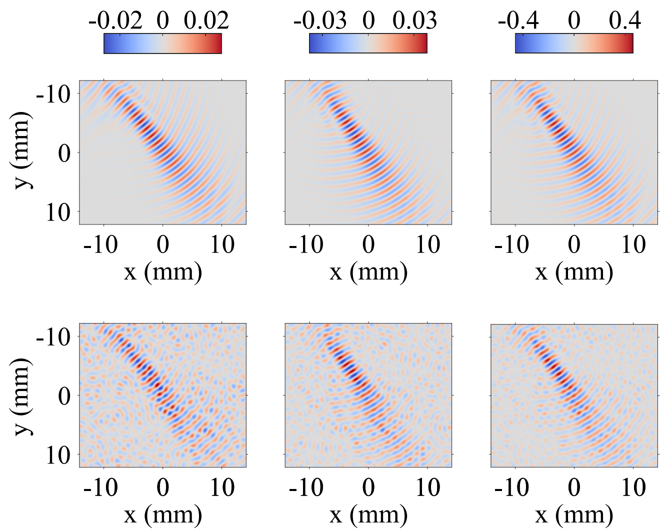

FIG. 7. (Color online) From left to right: the optical flow fields u and v, and the potential flow field P. Shown on the top are the true fields and on the bottom are the corresponding HS-u, HS-v, and PF estimates using the Helmholtz regularization. Fields are shown for the obliquely propagating field at a rotation angle of 45°. Colorbar units from left to right: m, m, and m^2.

C. Standing wave ultrasound field

Fig. 9 shows the true and the estimated optical flow fields HS-u, HS-v, and the potential flow estimate PF for the standing wave ultrasound field when using the Helmholtz regularization. The REs for the optical and potential flow estimates using the Laplace and the Helmholtz regularizations are shown in Table II. The Helmholtz regularized PF estimate has the smallest RE, followed by HS-v. Both of them appear similar to their corresponding true fields. The horizontal displacement magnitudes are lower than the vertical displacement magnitudes. This leads to greater artefacts in the HS-u estimate, seen by the high RE and visual inspection of the region of interest.

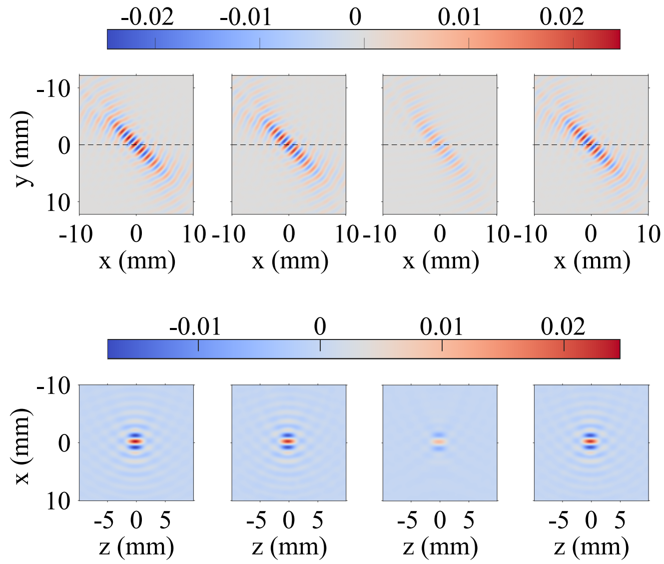

FIG. 8. (Color online) Coronal planes (top) and axial planes (bottom) of the obliquely propagating field. From left to right: true pressure field, PE-u, PE-v, and PE-P estimates when the Helmholtz regularization is used. Axial plane sections are shown by dashed lines on coronal planes. Colorbar units are in Pa.

Fig. 10 shows the true pressure field, PE-u, PE-v, and PE-P estimates on the coronal planes yx ($z = 0$ mm) and the axial planes xz ($y = 0$ mm) when using the Helmholtz regularization. Table II shows REs of the estimates when the Laplace and Helmholtz regularizations are used. The Helmholtz regularized PE-P has the lowest RE, followed by the RE of PE-v. On the coronal plane near the ultrasound transducer, PE-P and PE-u resemble the local high-amplitude focus regions well, whereas PE-v has smaller amplitudes. On the other hand, PE-u has lower amplitudes when approaching the steel layer. Inspection of the axial plane shows coarser but more accurate pressure values for PE-P and smoother but lower pressure values for PE-v.

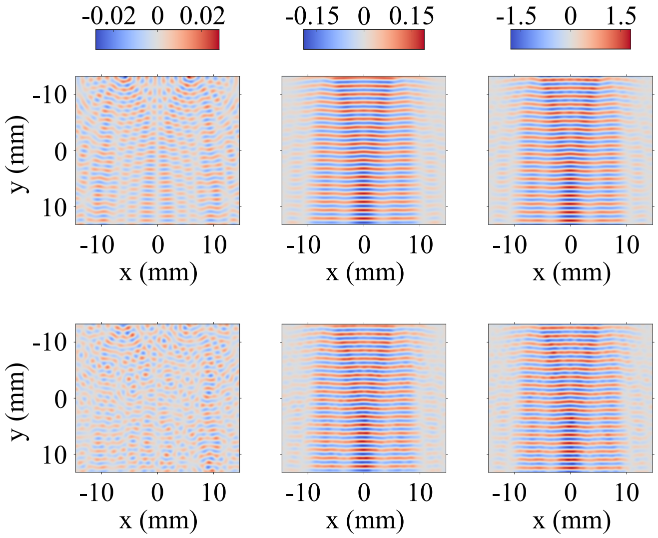

FIG. 9. (Color online) From left to right: the optical flow fields u and v, and the potential flow field P. Shown on the top are the true fields and on the bottom are the corresponding HS-u, HS-v, and PF estimates using the Helmholtz regularization. Fields are shown for the standing wave-field at a rotation angle of 45°. Colorbar units from left to right: m, m, and m^2.

V. DISCUSSION

In this work, two acoustic pressure estimation methods for SST were introduced. The pressure estimation methods are based on regularized least squares optical and potential flow optimizations. These methods allow promotion of smooth solutions via Laplace regularization or acoustic wave-like features via Helmholtz regularization. The pressure estimation approaches were tested using numerical simulations for a focused, an obliquely propagating focused, and a standing wave ultrasound fields. The pressure estimation methods were compared quantitatively and qualitatively to a previously introduced method (See Ref.[18]).

The results show that the Helmholtz regularization is more accurate than the Laplace regularization when estimating optical and potential flow. In this work, the Helmholtz

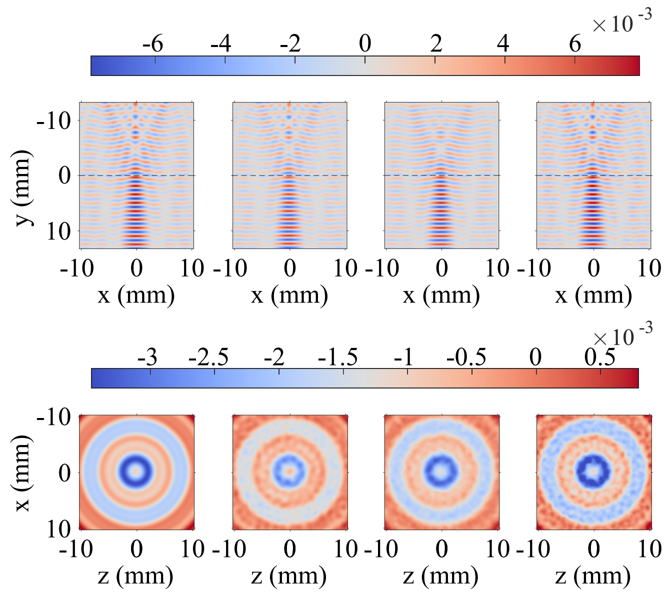

FIG. 10. (Color online) Coronal planes (top) and axial planes (bottom) of the standing wave-field. From left to right: true pressure field, PE-u, PE-v, and PE-P estimates when the Helmholtz regularization is used. Axial plane sections are shown by dashed lines on coronal planes. Colorbar units are in Pa.

prior was imposed as a soft constraint in a regularized least squares problem. While the distortions are not strictly pressure waves, they inherit the wave-like nature of the pressure wave. Several other studies have used the Helmholtz prior both as soft and hard constaints and support the suggestion that it is effective in reconstructing pressure fields using optically measured data as an input.[9,44,45] However, it should be noted that, since discretization affects regularization, Helmholtz regularization may not be optimal if a low discretization is used.

Furthermore, the results indicate that the potential flow based pressure estimation method PE-P with the Helmholtz regularization is the most accurate in estimating arbitrary ultrasound propagation. In comparison to a typical hydrophone measurement uncertainty of 10 %,[46] the PE-P pressure estimates are comparable to it with an average relative error of 15.8 % for the studied pressure fields.

When comparing PE-P estimates to PE-u and PE-v estimates, PE-P outperforms them in feasibility too. Although, PE-u and PE-v both use the HS algorithm to estimate the horizontal or vertical displacement components, they require different regularizations for optimal estimates depending on the propagation direction of the ultrasound beam. When the propagation angle of ultrasound is small with respect to the rotation axis of the camera, estimation accuracy of the horizontal component reduces and hence affects the accuracy of PE-u. For the vertical component, a small propagation angle is optimal. Accuracy of PE-v is affected by both the accuracy of the vertical component and directly of the propagation angle of the ultrasound. This is due to the plane-wave approximation that assumes ultrasound propagation along the rotation axis. Thus, while PE-P is more robust in comparison to PE-u and PE-v, it also performs similarly or better in accuracy.

In addition to accuracy of PE-P, it is based on estimating only one scalar potential flow field, and thus it is faster than estimating two optical flow components. Estimating 180 images in average took approximately 474 minutes for the optical flow fields and 81 minutes for the potential flow fields, that is over 5.8 times faster. The computations were implemented using MATLAB R2017b on a workstation equipped with 2.53 GHz Xeon E5649 (Intel Corporation, Santa Clara, CA) processor. The computational time for image processing can be further reduced utilizing parallel computing.

While this study concentrated on estimating ultrasound fields, the proposed new methods, PE-u and PE-P, can be adopted for estimating non-acoustically induced refractive index field as well. PE-u assumes that the refractive index field has a gradient along the plane perpendicular to the rotational imaging axis. For PE-P however, it is intrinsic that the refractive index field can be expressed using a scalar potential. This limits the method to applications with curl-free refractive index fields.[28] In comparison, the previously introduced method PE-v explicitly approximates the refractive index field as a wave-field. Thus, the new estimation methods can be thought as more general approaches.

The regularization parameter was not optimized but it was selected qualitatively by inspecting the estimates at a range of different regularization parameter values and choosing an estimate resembling a wave-field the most. This mimics conventional approach for choosing the regularization parameter. In comparison to Laplace regularization, Helmholtz regularization is much less sensitive to the choice of the regularization parameter as it was easier to narrow down a qualitatively optimal regularization parameter (results omitted). Classical regularization parameter selection methods, such as L-curve[47] and generalized cross-validation[48] methods exist but were not found suitable for this study (results omitted): an algorithm for this would benefit in selecting the parameter faster and more consistently. No thorough optimization for the imaged target was made. Optimizing the imaged target, such as the lattice spacing of details, could possibly improve the results.

ACKNOWLEDGMENTS

This work has been supported by the Academy of Finland (Projects 286247, 314411, and 312342 Centre of Excellence in Inverse Modelling and Imaging) and Jane and Aatos Erkko Foundation.

REFERENCES

[1]T. L. Szabo, *Diagnostic Ultrasound Imaging : Inside Out* (Academic Press, London, 2004), pp. 1–576.

[2]M. C. L. Peek and F. Wu, "High-intensity focused ultrasound in the treatment of breast tumours," Ecancer **12**, 794 (2018).

[3]Y. Meng, Y. Huang, B. Solomon, K. Hynynen, N. Scantlebury, M. L. Schwartz, and N. Lipsman, "MRI-guided focused ultrasound thalamotomy for patients with medically-refractory essential tremor," J. Vis. Exp. (130), e56365 (2017).

[4]S. M. Chowdhury, T. Lee, and J. K. Willmann, "Ultrasound-guided drug delivery in cancer," Ultrasonography **36**(3), 171–184 (2017).

[5]S. P. Robinson, "Hydrophones," in *Output Meas. Med. Ultrasound*, edited by R. C. Preston (Springer, London, 1991), Chap. 4.

[6]S. Maruvada, Y. Liu, J. E. Soneson, B. A. Herman, and G. R. Harris, "Comparison between experimental and computational methods for the acoustic and thermal characterization of therapeutic ultrasound fields," J. Acoust. Soc. Am. **137**(4), 1704–1713 (2015).

[7]Z. Xu, H. Chen, X. Yan, M.-L. Qian, and Q. Cheng, "Three-dimensional reconstruction of nonplanar ultrasound fields using Radon transform and the schlieren imaging method," J. Acoust. Soc. Am. **142**(1), EL82–EL88 (2017).

[8]Z. Xu, H. Chen, X. Yan, M. L. Qian, and Q. Cheng, "Quantitative calibration of sound pressure in ultrasonic standing waves using the schlieren method," Opt. Exp. **25**(17), 20401–20409 (2017).

[9]N. Chitanont, K. Yatabe, K. Ishikawa, and T. Oikawa, "Spatio-temporal filter bank for visualizing audible sound field by Schlieren method," Appl. Acoust. **115**, 109–120 (2017).

[10]R. Miyasaka, S. Harigane, S. Yoshizawa, and S. Umemura, "Quantitative measurement of highly focused ultrasound pressure field by optical shadowgraph," J. Phys. Conf. Ser. **520**(1), 012026 (2014).

[11]Y. Iijima and N. Kudo, "Evaluation of Frequency-dependent ultrasound attenuation in transparent medium using focused shadowgraph technique," Jpn. J. Appl. Phys. **56**(7), 07JF13 (2017).

[12]N. Kudo, "A simple technique for visualizing ultrasound fields without Schlieren optics," Ultrasound Med. Biol. **41**(7), 2071–2081 (2015).

[13]F. Nicolas, V. Todoroff, A. Plyer, G. Le Besnerais, D. Donjat, F. Micheli, F. Champagnat, P. Cornic, and Y. Le Sant, "A direct approach for instantaneous 3D density field reconstruction from background-oriented schlieren (BOS) measurements," Exp. Fluids **57**(1), 13 (2016).

[14]M. Kremer, C. Caskey, and W. Grissom, "Background-oriented schlieren imaging and tomography for rapid measurement of FUS pressure fields: initial results," J. Ther. Ultrasound **3**(Suppl 1), P68 (2015).

[15]E. Goldhahn and J. Seume, "The background oriented schlieren technique: Sensitivity, accuracy, resolution and application to a three-dimensional density field," Exp. Fluids **43**(2-3), 241–249 (2007).

[16]N. Taberlet, N. Plihon, L. Auzémery, J. Sautel, G. Panel, and T. Gibaud, "Synthetic schlieren - Application to the visualization and characterization of air convection," Eur. J. Phys. **39**(3), 035803 (2018).

[17]I. Butterworth and A. Shaw, "Realtime acousto-optical QA methods for high intensity fields," in *Proc. 39th Annu. Symp. Ultrason. Ind. Assoc.* (IEEE, New York, 2010), pp. 1–5.

[18]A. Pulkkinen, J. J. Leskinen, and A. Tiihonen, "Ultrasound field characterization using synthetic schlieren tomography," J. Acoust. Soc. Am. **141**(6), 4600–4609 (2017).

[19]G. S. Settles and M. J. Hargather, "A review of recent developments in schlieren and shadowgraph techniques," Meas. Sci. Technol. **28**(4), 042001 (2017).

[20]M. Raffel, "Background-oriented schlieren (BOS) techniques," Exp. Fluids **56**(3), 60 (2015).

[21]G. Caliano, A. S. Savoia, and A. Iula, "An automatic compact Schlieren imaging system for ultrasound transducer testing," IEEE Trans. Ultrason. Ferroelectr. Freq. Control **59**(9), 2102–2110 (2012).

[22]G. Meier, "Computerized background-oriented schlieren," Exp. Fluids **33**(1), 181–187 (2002).

[23]S. B. Dalziel, G. O. Hughes, and B. R. Sutherland, "Whole-field density measurements by 'synthetic schlieren'," Exp. Fluids **28**(4), 322–335 (2000).

[24]B. D. Lucas and T. Kanade, "An iterative image registration technique with an application to stereo vision," in *Proc. 7th Int. Jt. Conf. Artif. Intell. - Vol. 2* (Morgan Kaufmann,

San Francisco, 1981), pp. 674–679.

[25]B. K. Horn and B. G. Schunck, “Determining optical flow,” Artif. Intell. **17**(1-3), 185–203 (1981).

[26]L. Venkatakrishnan and G. E. A. Meier, “Density measurements using the Background Oriented Schlieren technique,” Exp. Fluids **37**(2), 237–247 (2004).

[27]B. Atcheson, W. Heidrich, and I. Ihrke, “An evaluation of optical flow algorithms for background oriented schlieren imaging,” Exp. Fluids **46**(3), 467–476 (2009).

[28]A. Luttman, E. M. Bollt, R. Basnayake, S. Kramer, and N. B. Tufillaro, “A framework for estimating potential fluid flow from digital imagery,” Chaos An Interdiscip. J. Nonlinear Sci. **23**(3), 033134 (2013).

[29]T. A. Pitts and J. F. Greenleaf, “Three-dimensional optical measurement of instantaneous pressure.,” J. Acoust. Soc. Am. **108**(6), 2873–2883 (2000).

[30]A. Torras-Rosell, S. Barrera-Figueroa, and F. Jacobsen, “Sound field reconstruction using acousto-optic tomography,” J. Acoust. Soc. Am. **131**(5), 3786–3793 (2012).

[31]M. Born and E. Wolf, “Foundations of geometrical optics,” in *Princ. Opt.*, 7 ed. (Cambridge University Press, Cambridge, 1999), Chap. 3.

[32]B. R. Sutherland, S. B. Dalziel, G. O. Hughes, and P. F. Linden, “Visualization and measurement of internal waves by ’synthetic schlieren’. Part 1. Vertically oscillating cylinder,” J. Fluid Mech. **390**, 93–126 (1999).

[33]A. Bruhn, J. Weickert, and C. Schnörr, “Lucas/Kanade meets Horn/Schunck: Combining local and global optic flow methods,” Int. J. Comput. Vis. **61**(3), 211–231 (2005).

[34]J. Kaipio and E. Somersalo, “Classical Regularization Methods,” in *Stat. Comput. Inverse Probl.* (Springer, New York, 2005), Chap. 2.

[35]T. J. Chung, “Introduction,” in *Comput. Fluid Dyn.* (Cambridge University Press, Cambridge, 2002), Chap. 1.

[36]A. Tarantola, “The Least-Squares Criterion,” in *Inverse Probl. Theory Methods Model Param. Estim.* (Society for Industrial and Applied Mathematics, Philadelphia, PA, 2005), Chap. 3.

[37]P. M. Morse and K. U. Ingard, “Acoustic wave motion,” in *Theor. Acoust.* (Princeton University Press, Princeton, NJ, 1968), Chap. 6.

[38]T. J. Chung, “Solution Methods of Finite Difference Equations,” in *Comput. Fluid Dyn.* (Cambridge University Press, Cambridge, 2002), Chap. 4.

[39]A. C. Kak and M. Slamey, “Algorithms for Reconstruction with Nondiffracting Sources,” in *Princ. Comput. Tomogr. Imaging* (IEEE, New York, 1988), Chap. 3.

[40]S. R. Deans, “Definition of the Radon transform,” in *Radon Transform Some Its Appl.* (John Wiley & Sons, New York, 1983), Chap. 2.

[41]S. R. Deans, “Recent Development of Inversion Methods,” in *Radon Transform Some Its Appl.* (John Wiley & Sons, New York, 1983), Chap. 6.

[42]B. E. Treeby and B. T. Cox, “k-Wave: MATLAB toolbox for the simulation and reconstruction of photoacoustic wave-fields,” J. Biomed. Opt. **15**(2), 021314 (2010).

[43]J. Kaipio and E. Somersalo, “Inverse Problems and Interpretation of Measurements,” in *Stat. Comput. Inverse Probl.* (Springer, New York, 2005), Chap. 1.

[44]K. Yatabe and T. Oikawa, "Optically visualized sound field reconstruction using Kirchhoff-Helmholtz equation," Acoust. Sci. Tech. **36**(4), 351–354 (2015).

[45]K. Yatabe, K. Ishikawa, and T. Oikawa, "Acousto-optic back-projection: Physical-model-based sound field reconstruction from optical projections," J. Sound Vib. **394**, 171–184 (2017).

[46]R. Preston, D. Bacon, S. Corbett, G. Harris, P. Lewin, J. McGregor, W. O'Brien, and T. Szabo, "Interlaboratory comparison of hydrophone calibrations," IEEE Trans. Ultrason. Ferroelectr. Freq. Control **35**(2), 206–213 (1988).

[47]P. C. Hansen, "Analysis of discrete ill-posed problems by means of the L-curve," SIAM Rev. **34**(4), 561–580 (1992).

[48]G. H. Golub, M. Heath, and G. Wahba, "Generalized cross-validation as a method for choosing a good ridge parameter," Technometrics **21**(2), 215–223 (1979).

TABLE I. Acoustic simulation parameters. Grid step Δh, time step Δt, pixels per wavelength (PPW), Courant-Friedrichs-Lewy (CFL) condition,[42] speed of sounds SOS_w and SOS_s, and densities ρ_w and ρ_s in water and steel.

Parameter	Δh	Δt_w [a]	Δt_s [b]	PPW	CFL
Value	147.2 μm	29.70 ns	9.75 ns	10 px	3
Parameter	$\mathrm{SOS_w}$	$\mathrm{SOS_s}$	ρ_w	ρ_s	
Value	1487 $\frac{\mathrm{m}}{\mathrm{s}}$	4529 $\frac{\mathrm{m}}{\mathrm{s}}$	1000 $\frac{\mathrm{kg}}{\mathrm{m}^3}$	7800 $\frac{\mathrm{kg}}{\mathrm{m}^3}$	

[a] The time step in the focused ultrasound field simulation is calculated based on SOS_w.

[b] The time step in the standing wave-field simulation is calculated based on SOS_s.

TABLE II. Relative errors (RE) in percentage for the Laplace and the Helmholtz regularized optical flow estimates HS-u and HS-v, potential flow estimate PF, and the consecutive pressure estimates PE-u, PE-v, and PE-P for the focused ultrasound field (Focused), the oblique propagating focused ultrasound field (Oblique), and the standing wave ultrasound field (Standing).

Field	**Regularization**	**HS-u**	**HS-v**	**PF**
Focused	Laplace	136.4	44.4	83.7
	Helmholtz	70.0	24.6	26.6
Oblique	Laplace	64.1	66.2	114.5
	Helmholtz	35.9	33.9	26.6
Standing	Laplace	169.1	16.6	34.4
	Helmholtz	59.9	10.0	9.0
Field	**Regularization**	**PE-u**	**PE-v**	**PE-P**
Focused	Laplace	34.0	43.4	39.5
	Helmholtz	17.5	19.8	18.8
Oblique	Laplace	38.7	66.4	34.2
	Helmholtz	16.0	61.8	13.9
Standing	Laplace	33.9	36.9	34.4
	Helmholtz	28.4	18.5	14.7

Figure captions:

Fig. 1. Schematic image of a synthetic schlieren setup.

Fig. 2. Schematic image of measurement setup of SST. Laboratory coordinates (x, y, z) of the pressure field, local coordinates (x', y, z') of the rotating camera, and the imaged target at a projection angle θ_n.

Fig. 3. Schematic image of simulation setups for a focused (left), an obliquely propagating focused (middle), and a standing wave (right) ultrasound fields. Borders of perfectly matched layers are shown by dashed lines.

Fig. 4. From left to right: Noisy unperturbed, perturbed, and their difference image for the focused ultrasound field. Shown on the top row are full-sized images and on the bottom row are the zoomed images.

Fig. 5. (Color online) From left to right: the optical flow fields u and v, and the potential flow field P. Shown on the top are the true fields and on the bottom are the corresponding HS-u, HS-v, and PF estimates using the Helmholtz regularization. Fields are shown for the focused ultrasound field at a rotation angle of 45°. Colorbar units from left to right: m, m, and m^2.

Fig. 6. (Color online) Coronal planes (top) and axial planes (bottom) of the focused ultrasound field. From left to right: true pressure field, PE-u, PE-v, and PE-P estimates when the Helmholtz regularization is used. Axial plane sections are shown by dashed lines on coronal planes. Colorbar units are in Pa.

Fig. 7. (Color online) From left to right: the optical flow fields u and v, and the potential flow field P. Shown on the top are the true fields and on the bottom are the corresponding HS-u, HS-v, and PF estimates using the Helmholtz regularization. Fields are shown for the obliquely propagating field at a rotation angle of 45°. Colorbar units from left to right: m, m, and m^2.

Fig. 8. (Color online) Coronal planes (top) and axial planes (bottom) of the obliquely propagating field. From left to right: true pressure field, PE-u, PE-v, and PE-P estimates when the Helmholtz regularization is used. Axial plane sections are shown by dashed lines on coronal planes. Colorbar units are in Pa.

Fig. 9. (Color online) From left to right: the optical flow fields u and v, and the potential flow field P. Shown on the top are the true fields and on the bottom are the corresponding HS-u, HS-v, and PF estimates using the Helmholtz regularization. Fields are shown for the standing wave-field at a rotation angle of 45°. Colorbar units from left to right: m, m, and m^2.

Fig. 10. (Color online) Coronal planes (top) and axial planes (bottom) of the standing wave-field. From left to right: true pressure field, PE-u, PE-v, and PE-P estimates when the Helmholtz regularization is used. Axial plane sections are shown by dashed lines on coronal planes. Colorbar units are in Pa.